Chinese Journal of Natural Medicines

Neuroprotective and antidiabetic lanostane-type triterpenoids from the fruiting bodies of *Ganoderma theaecolum*

Jiaocen Guo, Li Yang, Luting Dai, Qingyun Ma, Jiaoyang Yan, Qingyi Xie, Yougen Wu, Haofu Dai, Youxing Zhao

Citation: Jiaocen Guo, Li Yang, Luting Dai, Qingyun Ma, Jiaoyang Yan, Qingyi Xie, Yougen Wu, Haofu Dai, Youxing Zhao, Neuroprotective and antidiabetic lanostane-type triterpenoids from the fruiting bodies of *Ganoderma theaecolum*, Chinese Journal of Natural Medicines, 2025, 23(2), 245-256. doi: 10.1016/S1875-5364(25)60828-4.

View online: https://doi.org/10.1016/S1875-5364(25)60828-4

Chinese Journal of Natural Medicines 23 (2025) 245-256

Contents lists available at ScienceDirect

Chinese Journal of Natural Medicines

journal homepage: www.cjnmcpu.com/

Original article

Neuroprotective and antidiabetic lanostane-type triterpenoids from the fruiting bodies of *Ganoderma theaecolum*

Jiaocen Guo[a,b], Li Yang[b], Luting Dai[b], Qingyun Ma[b], Jiaoyang Yan[a], Qingyi Xie[b], Yougen Wu[a,*], Haofu Dai[b,*], Youxing Zhao[b,*]

[a] *School of Breeding and Multiplication (Sanya Institute of Breeding and Multiplication), Hainan University, Sanya 572025, China*

[b] *Key Laboratory of Research and Development of Natural Product from Li Folk Medicine of Hainan Province & National Key Laboratory for Tropical Crop Breeding, Institute of Tropical Bioscience and Biotechnology, Chinese Academy of Tropical Agricultural Sciences, Haikou 571101, China*

ARTICLE INFO

Article history:
Received 4 April 2024
Revised 28 May 2024
Accepted 17 June 2024
Available online 20 February 2025

Keywords:
Ganoderma theaecolum
Lanostane nortriterpenoids
Neuroprotective effects
PTP1B
α-Glucosidase

ABSTRACT

Eight previously undescribed lanostane triterpenoids, including five nortriterpenoids with 26 carbons, ganothenoids A–E (**1**–**5**), and three lanostanoids, ganothenoids F–H (**6**–**8**), along with 24 known ones (**9**–**32**), were isolated from the fruiting bodies of *Ganodrma theaecolum*. The structures of the novel compounds were elucidated using comprehensive spectroscopic methods, including electronic circular dichroism (ECD) and nuclear magnetic resonance (NMR) calculations. Compounds **1**–**32** were assessed for their neuroprotective effects against H_2O_2-induced damage in human neuroblastoma SH-SY5Y cells, as well as their inhibitory activities against protein tyrosine phosphatase 1B (PTP1B) and *α*-glucosidase. Compound **4** demonstrated the most potent neuroprotective activity against H_2O_2-induced oxidative stress by suppressing G_0/G_1 phase cell cycle arrest, reducing reactive oxygen species (ROS) levels, and inhibiting cell apoptosis through modulation of B-cell lymphoma 2 protein (Bcl-2) and Bcl-2 associated X-protein (Bax) protein expression. Compounds **26**, **12**, and **28** exhibited PTP1B inhibitory activities with IC_{50} values ranging from 13.92 to 56.94 μmol·L^{-1}, while compound **12** alone displayed significant inhibitory effects on *α*-glucosidase with an IC_{50} value of 43.56 μmol·L^{-1}. Additionally, enzyme kinetic analyses and molecular docking simulations were conducted for compounds **26** and **12** with PTP1B and *α*-glucosidase, respectively.

1. Introduction

Ganoderma mushrooms, renowned as valuable traditional folk medicines and functional foods, have been extensively utilized for the prevention and treatment of various diseases including cancer, insomnia, bronchitis and chronic hepatitis, with a history spanning over 2000 years in China and other Asian countries [1, 2]. Previous phytochemical studies on *Ganoderma* fungi have led to the isolation of lanostane triterpenoids [3], meroterpenoids [4], polysaccharides [5], sterols [6], alkaloids [4], and phenolic compounds. Lanostane triterpenoids, the characteristic constituents of the fruiting bodies of *Ganoderma* fungi, are widely recognized for their diverse bioactivities including antitumor [7], antidiabetic [8], neuroprotective [9], anti-inflammatory [10], hepatoprotective [11], antitubercular [12], and immunity enhancing [13] effects, as well as their highly oxidized structures, which have garnered significant attention from medicinal chemists and pharmacologists. *Ganoderma theaecolum* (*G. theaecolum*) is an important medicinal and edible homologous mushroom that grows in tropical and temperate regions. In China, it is widely distributed in Hainan, Yunnan, and Guangxi Province. The fruiting body of *G. theaecolum* is commonly used to prepare soup, wine, and tea, or as a traditional folk medicine for the treatment and prevention of various diseases [14, 15] in Hainan. Previous studies on its fruiting bodies have demonstrated that lanostane triterpenoids [14] and meroterpenoids [16] are the main components, and their hepatoprotective and anti-inflammatory activities have been reported.

Neurodegenerative diseases, including Alzheimer's disease (AD), Parkinson's disease (PD), Huntington's disease (HD), and multiple sclerosis (MS), constitute a complex group of age-related disorders characterized by the progressive deterioration of neurons in the central nervous system [17, 18]. As global population aging intensifies, the prevalence of these neurodegenerative diseases is also rising. The primary symptoms of these disorders include memory loss, communication difficulties, and impaired learning ability [19], particularly affecting the elderly population and significantly impacting patients' health and quality of life.

Diabetes is a chronic, multifactorial metabolic disorder characterized by hyperglycemia, which can damage organs and lead to chronic complications such as nephropathy, retinopathy, and cardiovascular disease [20]. This condition poses a significant threat to human health and imposes a substantial economic burden on society and patients. *α*-Glucosidase, an essential enzyme in the small intestine epithelium, catalyzes the hydrolysis of carbohydrates into glucose [21]. Inhibition of *α*-glucosidase impedes carbohydrate digestion and glucose absorption, and *α*-glucosidase

* Corresponding author.
E-mail addresses: wygeng2003@163.com (Y. Wu); daihaofu@itbb.org.cn (H. Dai); zhaoyouxing@itbb.org.cn (Y. Zhao)

https://doi.org/10.1016/S1875-5364(25)60828-4

inhibitors can effectively reduce postprandial hyperglycemia, thus aiding in diabetes management [22]. Protein tyrosine phosphatase 1B (PTP1B), a negative regulator of the insulin signaling pathway, has been identified as a crucial therapeutic target for treating type 2 diabetes [23]. Inhibiting PTP1B enhances insulin sensitivity, making PTP1B inhibitors potential candidates for antidiabetic drug development [24]. Consequently, bioactive compounds exhibiting dual inhibition of α-glucosidase and PTP1B may offer enhanced therapeutic benefits in the treatment of type 2 diabetes.

Natural products derived from medicinal fungi have garnered significant research interest due to their extensive pharmacological activities and minimal adverse effects [7, 25]. As part of ongoing efforts to sexplore diverse chemical compositions and intriguing bioactivities from the *Ganodrma* fungus, a chemical study was conducted on the fruiting bodies of *G. theaecolum*. This investigation resulted in the isolation of eight novel lanostane triterpenoids (Fig. 1), comprising five nortriterpenoids ganothenoids A–E (**1**–**5**) and three triterpenoids ganothenoids F–H (**6**–**8**), along with 24 previously known compounds (**9**–**32**). Many of these triterpenoids exhibited neuroprotective effects and PTP1B/α-glucosidase inhibitory activities. This paper reports on the isolation, structural elucidation, neuroprotective effects, and α-glucosidase inhibitory activities of the triterpenoids extracted from the fruiting bodies of *G. theaecolum*.

2. Results and discussion

2.1. Structure elucidation

The molecular formula of **1** was determined to be $C_{26}H_{40}O_6$ based on high-resolution electrospray ionization mass spectrometry (HR-ESI-MS) ion peak at *m/z* 471.2729 $[M + Na]^+$ (Calcd. for 471.2717) and ^{13}C nuclear magnetic resonance (NMR) data. The infrared radiation (IR) spectrum exhibited absorption bands characteristic of double bond (1569 cm^{-1}), carboxyl (1656 cm^{-1}), α,β-unsaturated carbonyl (1723 cm^{-1}), and hydroxyl (3418 cm^{-1}) groups. The ^1H NMR data (Table 2) of **1** indicated the presence of six methyls (δ_H 0.99, 1.28, 0.98, 1.03, 0.85, and 1.26), and three oxygenated methines (δ_H 3.17, 4.54, and 4.81). Analysis of the distortionless enhancement by polarization transfer (DEPT) and heteronuclear single quantum coherence (HSQC) spectra revealed that the 26 carbon signals in the ^{13}C NMR data (Table 1) could be classified as six methyls, six methylenes, six methines (three oxygenated at δ_C 79.0, 70.2, and 73.2), and eight quaternary carbons (including one α,β-unsaturated ketone group at δ_C 161.3, 143.1, and 202.4, and one carboxyl at δ_C 177.0). Comparison of these 1D NMR data with those of ganodernoid B [26] indicated a close structural similarity, suggesting that **1** was a lanostane nor-triterpenoid. The primary difference between them was the presence of an additional methylene (CH_2-22) in the side chain of **1**, supported by heteronuclear multiple bond correlation (HMBC) correlations (Fig. 2) from H_3-21 (δ_H 0.98) and H-17 (δ_H 1.90) to C-20 (δ_C 35.2) and C-22 (δ_C 42.4), and ^1H-^1H COSY cross-peaks (Fig. 2) of H-20 (δ_H 1.94)/H_2-22 (δ_H 2.40). Additionally, two ketone groups attached at C-3 and C-15 in ganodernoid B were reduced to two oxymethine groups in **1**, as confirmed by HMBC correlations from H_3-28 (δ_H 1.03) and H_3-29 (δ_H 0.85) to C-3 (δ_C 78.9), from H_3-30 (δ_H 1.26) and H-16 (δ_H 2.13) to C-15 (δ_C 73.2), and ^1H-^1H COSY correlations of H_2-1/H_2-2/H-3 and H-15/H_2-16/H-17. Further analysis of the ^1H-^1H COSY and HMBC correlations (Fig. 2) confirmed the planar structure of **1** as depicted in Fig. 1.

The relative configuration of the tetracyclic structure of **1** was elucidated through rotating frame overhauser effect spectroscopy (ROESY) spectrum analysis (Fig. 3). ROESY correlations (Fig. 3) between H-3/H-5, H_3-29/H-7, and H-7/H_3-30/H-17 indicated that these protons were positioned on the same side of the molecule and assigned as α-oriented. Conversely, CH_3-28, CH_3-19, and H-15 were designated as β-oriented based on the ROESY cross-peaks of H_3-19/H_3-28 and H_3-18/H-15 (Fig. 3). The relative configuration of C-20 in the side chain was determined through ^1H and ^{13}C NMR chemical shift calculations. The calculated ^{13}C and ^1H NMR chemical shifts of **1a** (3*R*,5*R*,7*S*,10*S*,13*R*,14*R*,15*S*,17*S*,20*R*) demonstrated better agreement with the experimental values (see Supplementary material), exhibiting a higher correlation coefficient (R^2) and lower mean absolute error (MAE) and corrected mean absolute error (CMAE) values compared to those of **1b** (3*R*,5*R*,7*S*,10*S*,13*R*,14*R*,15*S*,17*S*,20*S*). Furthermore, DP4+ analysis predicted **1a** as the most probable candidate structure with a 100% probability for the ^{13}C NMR data. The calculated electronic circular dichroism (ECD) curve (Fig. 4) for **1** corresponded well with the experimental ECD curve, indicating its absolute configuration as 3*R*,5*R*,7*S*,10*S*,13*R*,14*R*,15*S*,17*S*,20*R*. In the ECD spectrum of **1**, a strong positive Cotton effects (CE) at 241 nm ($\Delta\varepsilon$ = 6.59) for a π-π^* electron transition and a weak negative CE at 352 ($\Delta\varepsilon$ = −1.02) nm for a n-π^* electron transition suggested 13*R*,14*R* configuration based on the octant rule for the α,β-unsaturated ketone group [27]. Consequently, the structure of **1** was identified as 24,25,26,27-tetranorlanost-3β,7β,15α-trihydroxy-11-oxo-8-en-23-oic acid and named ganothenoid A.

The molecular formula of **2** was determined to be $C_{26}H_{38}O_6$ based on its HR-ESI-MS and ^{13}C NMR spectrum, indicating eight degrees of unsaturation. Comprehensive analysis of the 1D and 2D NMR data (Tables 1 and 2) revealed that **2** was structurally similar to **1**. The primary distinction between the two compounds was the presence of a ketone group at C-15 (δ_C 217.2) in **2**, rather than the hydroxylated methine group (δ_C 73.2) observed in **1**. This structural difference was confirmed by HMBC correlations from H_3-30 (δ_H 1.38), H-17 (δ_H 2.21) and H_2-16 (δ_H 2.19) to C-15 (δ_C 217.2). Compound **2** exhibited the same relative configuration as **1**, as evidenced by ROESY correlations (Fig. 3) of H-3/H-5/H-7/H_3-30/H-17 and H_3-18/H_3-19/H_3-28. The comparable large coupling constant of H-20/H-22 (d, J = 6.2 Hz) and ^{13}C NMR chemical shifts of the side chain from C-20 to C-23 with those of **1** indicated an R^*-configuration of C-20 for **2**. The identical absolute configuration of **2** and **1** was substantiated by similar ECD Cotton Effects at 253 nm and their specific rotations ($[\alpha]_D^{25}$ + 76 for **1**; $[\alpha]_D^{25}$ +99 for **2**) (Fig. 4). Consequently, **2** was characterized and designated as ganothenoid B.

Compound **3** was isolated as a yellow oil with the molecular formula $C_{26}H_{36}O_6$, as determined by ^{13}C NMR and HR-ESI-MS data (*m/z* $[M + Na]^+$ 467.2425, Calcd. for $C_{26}H_{36}NaO_6$ 467.2404). A detailed comparison of the ^1H and ^{13}C NMR spectra (Tables 1 and 2) of **3** and **2** indicated that they shared the same C-26 nor-triterpenoid skeleton, with the key difference being the oxidation of the oxymethine at C-7 in **2** to a ketone group (δ_C 199.9) in **3**. This structural deduction was confirmed by HMBC correlations from H-5 (δ_H 1.60), H_2-6 (δ_H 2.63), and H_3-30 (δ_H 1.54) to C-7 (δ_C 199.9). The planar structure of compound **3** was further corroborated by ^1H-^1H COSY and HMBC, as illustrated in Fig. 2. The relative configuration of **3** was established to be identical to that of **1** based on ROESY correlations (Fig. 3). The relative configuration of C-20 was determined to be R^* based on the similarity of 1D NMR data with those of **1**. Moreover, the absolute configuration of **3** was elucidated to be 3*S*,5*R*,10*S*,13*R*,14*R*,17*R*,20*R* through comparison of the experimental and calculated ECD curves (Fig. 4). Consequently, the structure of **3** was determined and named ganothenoid C.

A molecular formula $C_{26}H_{34}O_6$ for **4** was established by HR-ESI-MS (*m/z* 465.2267 $[M + Na]^+$, Calcd. for $C_{26}H_{34}NaO_6$ 465.2248). Comparative analysis of ^1H and ^{13}C NMR data

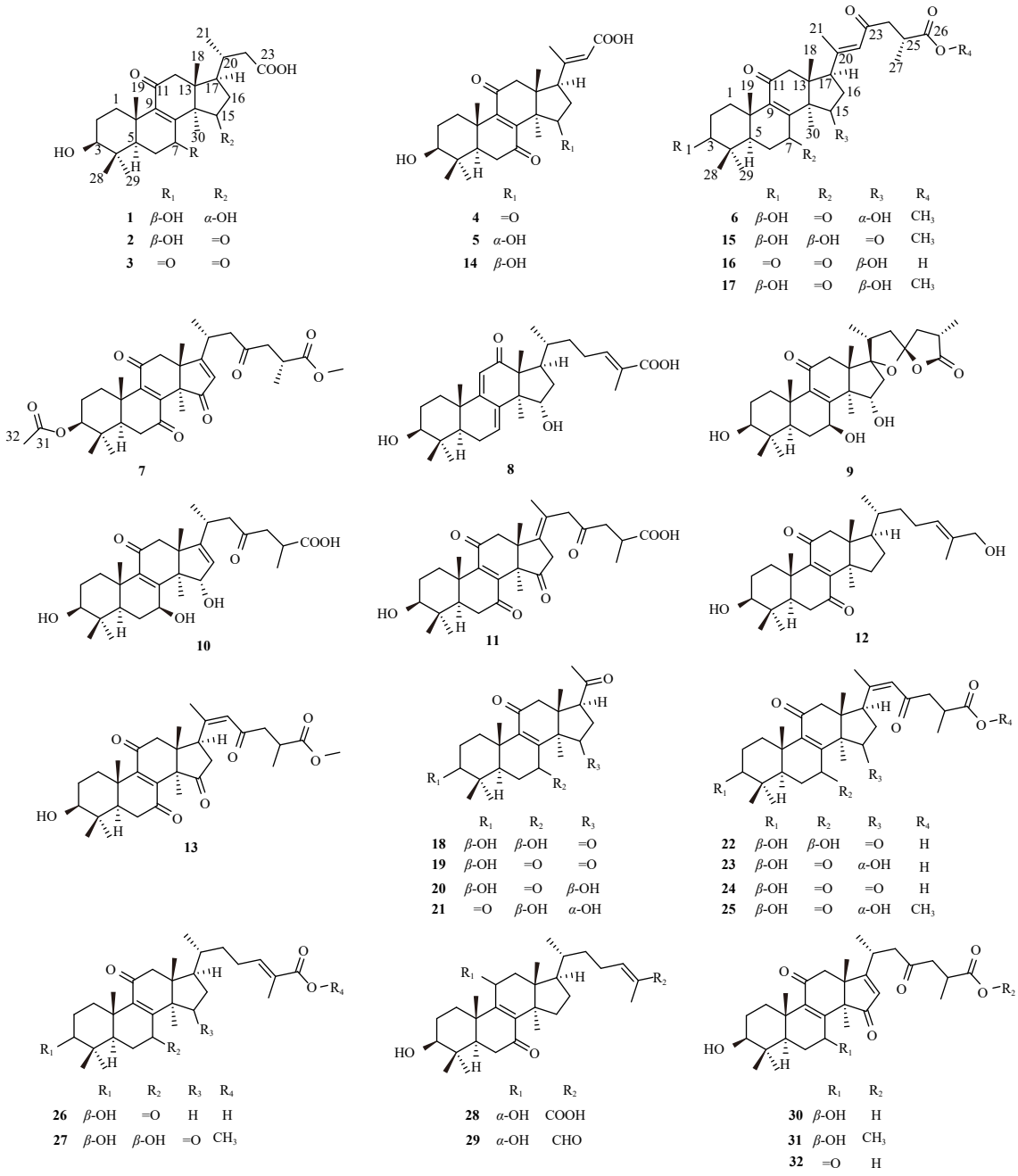

Fig. 1 Chemical structures of **1**–**32** isolated from *G. theaecolum.*

(Tables 1 and 2) of **4** with those of **3** indicated that they shared an identical tetracyclic core structure but differed in their C-20–C-23 side chain. The CH-20–CH_2-22 unit in **3** underwent dehydration to form a tri-substituted double bond $\Delta^{20(22)}$ in **4**. This was corroborated by HMBC correlations from H-17 (t, δ_H 3.25) and H_3-21 (s, δ_H 2.09) to C-20 (δ_C 154.8) and C-22 (δ_C 118.2) (Fig. 2), as well as from H-22 (s, δ_H 5.68) to C-21 (δ_C 19.9), C-17 (δ_C 54.3), and C-23 (δ_C 170.3). The relative configuration of **4** confirmed to be identical to that of **3** through ROESY correlations (Fig. 3). The *E* configuration of $\Delta^{20(22)}$ was determined by the ROESY correlation of H-22 with H-17. The experimental ECD curves (Fig. 4) of **4** aligned with the calculated ECD curves of (3*S*,5*R*,10*S*,13*R*,14*R*,17*R*)**-4**, thereby assigning the absolute configuration of **4** as 3*S*,5*R*,10*S*,13*R*,14*R*,17*R*. Consequently, the structure of **4** was elucidated as 3*β*-hydroxy-7,11,15-trioxolanost-8,20(22)*E*-dien-23-oic acid and designated as ganothenoid D.

Compound **5** was assigned a molecular formula of $C_{26}H_{36}O_6$ by HR-ESI-MS. A detailed comparison of 1D NMR data (Tables 1 and 2) with that of **4** indicated that **5** was also a lanostane nortriterpenoid with 26 carbons. The key distinction between the two compounds was the replacement of the ketone carbonyl at C-15 in **4** with a hydroxylated methine (δ_C 77.4) in **5**. This was evidenced by HMBC correlations (Fig. 2) from H_2-16 (δ_H 2.02) and H_3-30 (δ_H 1.24) to δ_C 77.4 (C-15) and ^1H-^1H COSY correlations from H-15/H_2-16/H-17. The ROE cross peak of H-22 with H-17 established the *E* configuration of the double bond $\Delta^{20(22)}$. In the ROESY spectrum of **5** (Fig 3), cross-peaks of H-3/H-5 and H_3-30/H-17 indicated that H-3, H-5, CH_3-30, and H-17 were located on the same face of the molecule. Conversely, ROESY cross-peaks of H_3-28/H_3-19/H_3-18/H-15 revealed these protons resided on the opposite face. The experimental ECD curves of **5** (Fig 4) corresponded well with the calculated curves of (3*S*,5*R*,10*S*,13*R*,14*R*,17*R*)-**5**, confirming its absolute configuration as 3*S*,5*R*,10*S*,13*R*,14*R*,17*R*. Consequently, compound **5** was identified and designated as gan-

Table 1 The ^{13}C NMR (125 MHz) spectroscopic data for compounds **1**–**8**.

No.	**1**[a]	**2**[a]	**3**[c]	**4**[b]	**5**[a]	**6**[a]	**7**[a]	**8**[b]
1	35.9, CH_2	36.0, CH_2	33.8, CH_2	33.3, CH_2	35.1, CH_2	35.3, CH_2	34.7, CH_2	34.6, CH_2
2	28.7, CH_2	28.3, CH_2	27.5, CH_2	27.1, CH_2	28.3, CH_2	28.2, CH_2	24.7, CH_2	27.3, CH_2
3	79.0, CH	78.9, CH	77.7, CH	75.3, CH	78.3, CH	78.2, CH	81.0, C	76.3, CH
4	39.7, C	39.4, C	39.2, C	38.7, C	40.1, C	39.9, C	38.8, C	38.4, C
5	50.4, CH	50.3, CH	50.9, CH	50.1, CH	52.0, CH	51.1, CH	50.4, CH	48.2, CH
6	29.0, CH_2	28.0, CH_2	36.4, CH_2	36.4, CH_2	37.5, CH_2	37.2, CH_2	35.9, CH_2	22.9, CH_2
7	70.2, CH	67.9, CH	199.9, C	199.6, C	205.7, C	207.2, C	199.8, C	130.5, CH
8	161.3, C	158.9, C	147.2, C	146.8, C	150.0, C	150.7, C	151.5, C	140.2, C
9	143.1, C	144.1, C	151.8, C	150.9, C	155.2, C	156.1, C	153.6, C	161.8, C
10	39.7, C	39.7, C	40.8, C	39.9, C	41.3, C	41.4, C	41.7, C	37.7, C
11	202.4, C	200.4, C	199.5, C	198.6, C	203.1, C	202.2, C	200.7, C	117.2, CH
12	53.1, CH_2	51.5, CH_2	49.7, CH_2	48.2, CH_2	52.5, CH_2	51.8, CH_2	45.5, CH_2	203.3, C
13	48.3, C	46.6, C	57.1, C	55.9, C	49.1, C	50.6, C	53.1, C	52.6, C
14	55.3, C	60.4, C	44.5, C	45.1, C	54.6, C	53.6, C	56.6, C	55.8, C
15	73.2, CH	217.2, C	207.7, C	207.1, C	77.4, CH	73.8, CH	205.4, C	71.4, CH
16	36.9, CH_2	41.8, CH_2	40.2, CH_2	36.4, CH_2	36.0, CH_2	32.7, CH_2	124.0, C	39.1, CH_2
17	49.3, CH	46.8, CH	45.2, CH	47.7, CH	54.3, CH	53.0, CH	185.5, C	41.2, CH
18	17.5, CH_3	17.8, CH_3	16.4, CH_3	17.4, CH_3	19.4, CH_3	19.2, CH_3	30.5, CH_3	15.1, CH_3
19	19.8, CH_3	18.9, CH_3	18.0, CH_3	17.3, CH_3	18.0, CH_3	17.6, CH_3	17.6, CH_3	21.8, CH_3
20	35.2, CH	34.4, CH	33.3, CH	154.8, C	159.2, C	157.7, C	30.1, CH	35.6, CH
21	19.8, CH_3	19.8, CH_3	19.7, CH_3	19.9, CH_3	20.9, CH_3	21.3, CH_3	20.0, CH_3	19.0, CH_3
22	42.2, CH_2	41.8, CH_2	40.6, CH_2	118.2, CH	118.5, CH	125.7, CH	48.4, CH_2	34.5, CH_2
23	177.0, C	175.0, C	176.9, C	167.3, C	170.3, C	200.8, C	208.9, C	25.3, CH_2
24						47.2, CH_2	47.1, CH_2	141.9, CH
25						36.4, CH	35.9, CH	127.5, C
26						178.2, C	178.0, C	168.8, C
27						17.3, CH_3	17.3, CH_3	12.1, CH_3
28	28.4, CH_3	16.2, CH_3	28.0, CH_3	27.7, CH_3	28.2, CH_3	28.2, CH_3	28.0, CH_3	16.2, CH_3
29	16.4, CH_3	28.7, CH_3	15.6, CH_3	15.7, CH_3	16.1, CH_3	16.0, CH_3	16.6, CH_3	28.1, CH_3
30	20.0, CH_3	24.9, CH_3	22.1, CH_3	22.0, CH_3	24.9, CH_3	20.6, CH_3	33.4, CH_3	18.3, CH_3
31							172.8, C	
32							21.1, CH_3	
-OCH_3						52.3, CH_3	52.4, CH_3	

[a] measured in MeOD, [b] measured in DMSO-d_6, [c] measured in $CDCl_3$.

othenoid E.

Compound **6** was isolated as a yellow oil. Its molecular formula was determined to be $C_{31}H_{44}O_7$ based on the molecular ion peak at *m/z* 551.2979 $[M + Na]^+$ (Calcd. for $C_{31}H_{44}O_7$, 551.2979), indicating ten degrees of unsaturation. Comparison of the ^1H and ^{13}C NMR data (Tables 1 and 2) of **6** and **17** [28] suggested that both compounds shared the same planar lanostane skeleton. The relative configuration of **6** was determined to be identical to **17**, except for C-15, through analysis of the ROESY correlations (Fig. 3). The ROESY cross-peak of H-3/H_3-29/H-5 indicated the same orientation of these protons, while the ROESY cross-peak of H-19/H_3-28 confirmed their position on the face opposite to H-3 (Fig. 3). The ROESY cross-peak of H_3-18/H-15 established their location on the same face of the molecule (Fig. 3). The *E* configuration of the $\Delta^{20(22)}$ double bond in **6** was determined by the ROESY cross-peaks of H-17 (δ_C 3.04) with H-22 (δ_C 6.25). The absolute configuration of the tetracyclic core structure of **6** was identified as identical to that of **5** based on their similar ECD spectra (Fig. 4). The absolute configuration of C-25 was determined to be the same as that of ganodapplanoic acid A, based on their similar chemical shifts [29]. Consequently, compound **6** was identified as 20(*E*)-3β,15α-dihydroxy-7,11,23-trioxolanost-8,20(22)-dien-26-oate and named ganothenoid F.

The molecular formula of compound **7** was determined to be

Table 2 H NMR (500 MHz, *J* in Hz) spectroscopic data for compounds **1**–**8**.

No.	1[a]	2[a]	3[c]	4[b]	5[a]	6[a]	7[a]	8[b]
1	2.70, dt (13.6, 3.5)	2.81, overlap	2.87, m	2.65, m	2.85, dt (9.7, 3.2)	2.83, dt (13.9, 3.8)	2.99, td (14.1, 6.2)	1.93, dt (13.1, 3.3)
	0.97, overlap	1.04, overlap	1.27, m	1.26, m	1.23, overlap	1.28, m	1.55, m	1.49, m
2	1.61, overlap	2.21, overlap	1.71, m	0.90, m	1.71, m	1.72, overlap	1.77, m	1.59, m
		1.56, m						
3	3.17, dd (11.6, 4.5)	3.17, dd (11.7, 4.7)	3.30, dd (11.6, 4.7)	3.05, dd (10.9, 5.6)	3.23, dd (11.6, 5.2)	3.23, dd (11.6, 4.8)	4.58, brd (5.4)	3.04, dd (9.9, 5.4)
5	0.96, dd (14.6, 5.8)	0.96, brd (12.9)	1.60, dd (9.2, 4.2)	1.55, dd (14.5, 2.7)	1.58, brd (15.4)	1.59, dd (15.0, 2.5)	1.92, dd (13.9, 4.7)	1.09, dd (11.8, 3.5)
6	2.13, dd (10.2, 7.5)	2.19, m	2.63, m	2.61, overlap	2.71, t (14.5)	2.72, m	2.62, m	2.22, dd (10.7, 3.9)
	1.65, m	1.60, m		2.42, dd overlap	2.53, d (5.6)	2.55, overlap		2.12, m
7	4.54, dd (10.0, 7.4)	4.85, brd (9.3)						6.45, brd (6.4)
11								5.49, s
12	2.89, d (15.3)	2.94, d (16.2)	2.90, d (15.7)	3.17, d (10.2)	3.00, d (15.1)	3.06, d (15.8)	3.19, d (16.7)	
	2.41, overlap	2.65, d (16.2)	2.70, d (15.7)	2.41, overlap	2.38, d (15.1)	2.34, d (15.8)	2.65, d (16.7)	
15	4.81, brd (8.2)				4.57, brd (7.3)	4.53, dd (9.8, 6.1)		4.30, dd (13.2, 7.1)
16	1.89, dd (12.9, 9.3)	2.80, overlap	2.78, dd (17.8, 8.8)	2.61, overlap	2.38, overlap	2.57, overlap	5.75, s	1.82, m
		2.19, m	2.05, m	2.42, dd overlap	2.02, dd (14.7, 9.2)	1.75, m		
17	1.90, m	2.21, overlap	2.22, dd (15.2, 8.6)	3.25, t (8.6)	2.87, m	3.04, dd (14.9, 9.3)		2.03, brd (7.4)
18	0.99, s	1.02, s	0.88, s	0.58, s	0.95, s	1.33, s	1.14, s	0.88, s
19	1.28, s	1.23, s	1.28, s	1.13, s	1.36, s	0.76, s	1.20, s	1.02, s
20	1.94, m	2.09, m	2.07, m				3.02, m	1.24, m
21	0.98, d (6.3)	1.08, d (6.2)	1.08, d (6.4)	2.09, s	2.17, s	2.09, s	1.15, d (7.0)	0.85, d (6.3)
22	2.40, overlap	2.41, brd (11.9)	2.42, dd (15.0, 3.5)	5.68, s	5.79, s	6.25, s	2.95, t (8.5)	1.35, m
	2.03, t (8.9)	2.16, m	2.20, m				2.76, dd (17.5, 5.7)	1.15, m
23								2.21, m
								2.08, m
24						2.92, m	2.94, t (8.5)	6.65, t (7.0)
						2.64, m	2.80, dd (17.1, 5.7)	
25						2.89, m	2.98, m	
27						1.18, d (7.1)	1.17, d (7.0)	1.74, s
28	1.03, s	1.04, s	0.91, s	0.91, s	1.02, s	0.90, s	1.04, s	0.81, s
29	0.85, s	0.86, s	1.04, s	0.78, s	0.90, s	1.02, s	0.97, s	0.93, s
30	1.26, s	1.38, s	1.54, s	1.47, s	1.24, s	1.25, s	1.50, s	0.83, s
32							2.07, s	
-OCH_3						3.67, s	3.65, s	

[a] measured in MeOD, [b] measured in DMSO-d_6, [c] measured in $CDCl_3$.

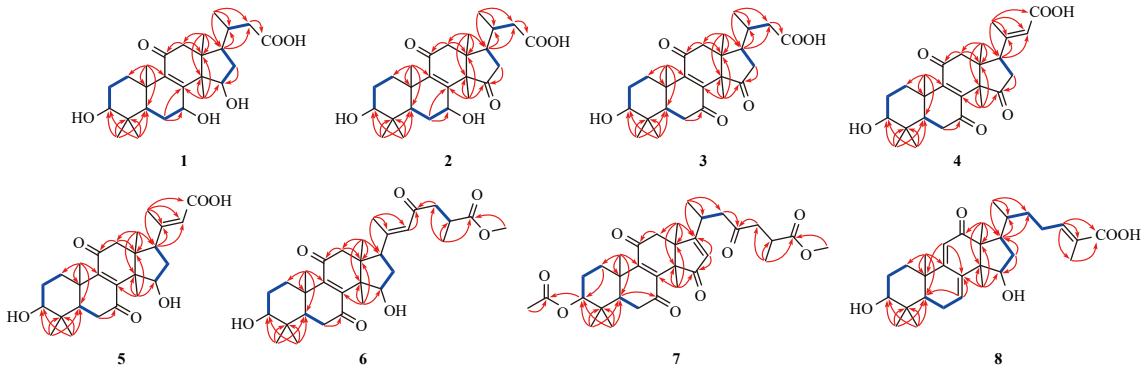

Fig. 2 Key HMBC (arrow) and ^{1}H-^{1}H COSY (bold line) correlations of **1**–**8**.

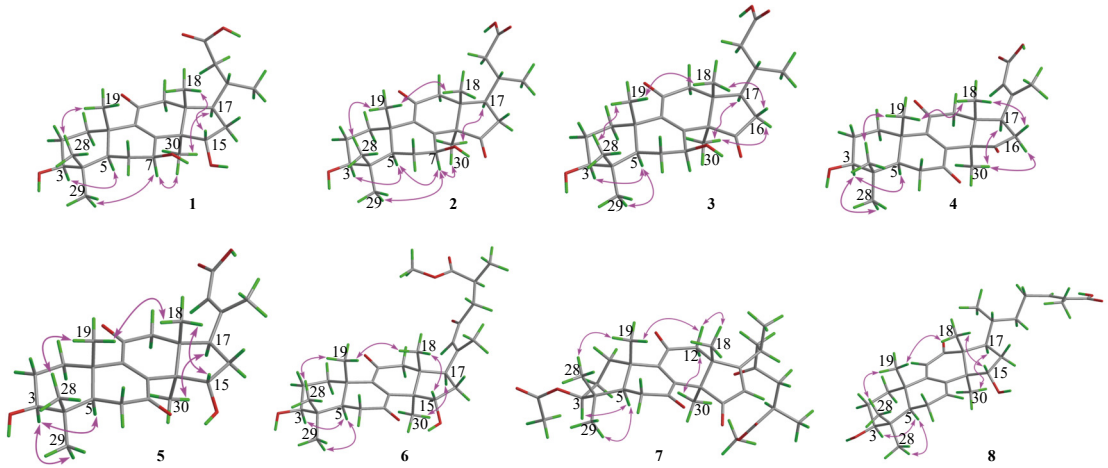

Fig. 3 Key ROESY (double arrows) correlations of **1**–**8**.

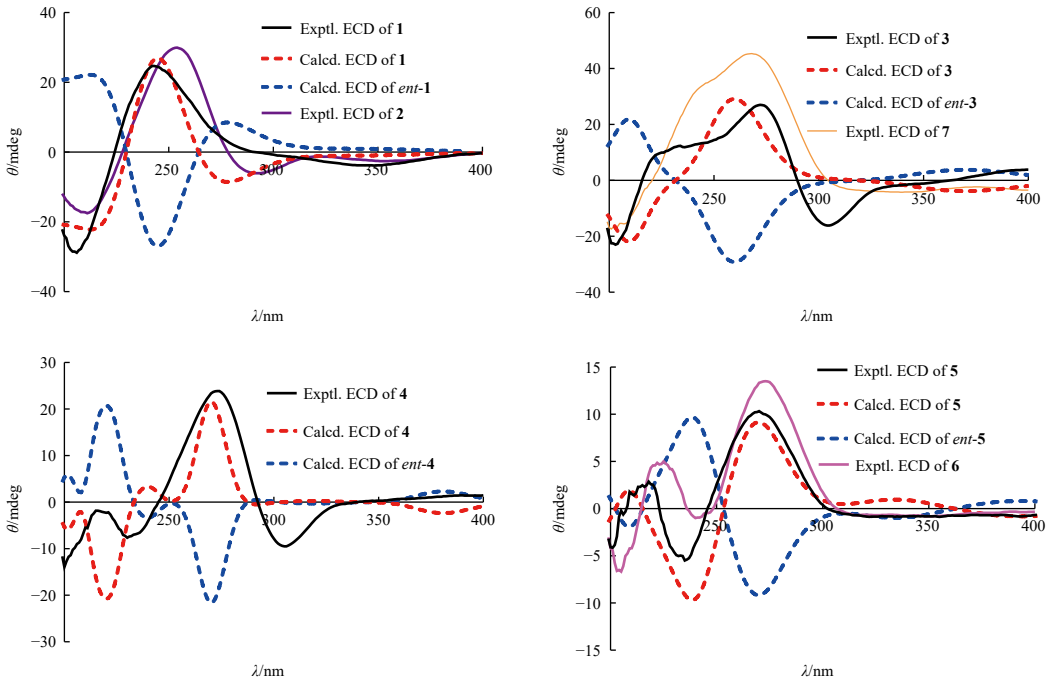

Fig. 4 Comparison of experimental and calculated ECD spectra of **1**–**7**.

$C_{33}H_{44}O_8$ based on its HR-ESI-MS ion peak at *m/z* 591.2939 [M + Na]$^+$ (Calcd. 591.2928). The ^{13}C NMR and HSQC spectra revealed 33 carbons, including nine methyls (one methoxyl), six methylenes, five methines (one olefinic and one oxygenated), and thirteen non-protonated carbons (three olefinic, four ketones, and two ester carbonyls). These 1D NMR data (Tables 1 and 2) indicated that the structure of **7** closely resembles that of **32** [30], with the addition of an acetyl and a methoxyl group in **7**. The HMBC

correlation from H-3 (δ_H 4.58) and the acetyl group protons (δ_H 2.07, 3H, s) to the carbonyl carbon (δ_C 172.8) suggested the acetyl group's attachment to C-3 (δ_C 81.0). Additionally, the methoxyl group was determined to be at C-26 by the HMBC correlation from methoxy protons (δ_H 3.65, 3H, s) to C-26 (δ_C 178.0). Thus, the planar structure of **7** was established as shown in Fig. 1. The ROESY correlations of H-3/H-5/H_3-29 and H-12α/H_3-30 revealed the *α*-orientation of these protons. Furthermore, CH_3-28, CH_3-19, and CH_3-18 were determined to be *β*-orientation based on the ROESY correlations of H_3-28/H_3-19 and H_3-18/H-12β/H_3-19. The similar ^{13}C NMR chemical shift of the C-20–C-23 side chain in **7** and **1** indicated an R^*-configuration for C-20. Based on similar chemical shifts and lanostane skeleton, the absolute configuration of C-25 in **7** was determined to be consistent with that of ganoleucoin *R* [31]. The similar ECD curves (Fig. 4) between compounds **7** and **3** indicated their shared absolute configuration. Therefore, the structure of **7** was defined as 3*β*-acetoxyl-7,11,15,23-tetraoxo-lanost-8,16-dien-26-oate and named ganothenoid G.

The molecular formula of compound **8** was determined as $C_{30}H_{44}O_5$ based on the $[M + Na]^+$ ion at *m/z* 507.3081 (Calcd. for $C_{30}H_{44}NaO_5$, 507.3102) in its HR-ESI-MS. Detailed analysis of the 1D NMR data (Tables 1 and 2) of **8** revealed a structure closely resembling that of ganodaustralic acid E [32]. The key difference was the replacement of a hydroxylated quaternary carbon at C-20 (δ_C 74.7) in ganodaustralic acid E by a methine group at C-20 (δ_C 35.6) in **8**. This structural difference was corroborated by HMBC correlations from H_3-21 (δ_H 0.85) to C-20, C-17 (δ_C 41.2), and C-22 (δ_C 34.5), and from H-17 (δ_H 2.03) to C-20, C-22, and C-16 (δ_C 39.1). The *E* configuration of the double bond Δ^{24} was determined by the ROESY correlation between H_3-27 and H_2-23 (Fig. 3). The relative configuration of **8** was identical to that of ganodustralic acid E, as evidenced by their similar NMR data (Fig. 3). The comparable ECD spectra and specific rotations of **8** and ganodaustralic acid E indicated the absolute stereochemistry of **8** as 3*S*,5*R*,10*S*,13*R*,14*S*,15*S*,17*S*,20*R*. Consequently, compound **8** was established as shown in Fig. 1 and named ganothenoid H.

Twenty-four known triterpenoids (Fig. 1) (**9**–**32**) were identified through comparison of their NMR data with those reported in the literature. These compounds include ganotropic acid (**9**) [33], 3*β*,7*β*,15*α*-trihydroxy-11,23-dioxo-lanost-8,16-dien-26-oic acid (**10**) [34], ganoderenic acid AM1 (**11**) [14], 11-oxo-lucidadiol (**12**) [35], methyl ganoderate H (**13**) [36], petchinoide A (**14**) [37], ganoderense C (**15**) [38], (20*E*)-15*β*-hydroxy-3,7,11,23-tetraoxolanost-8,20(22)-dien-26-oic acid (**16**) [28], (20*E*)-3*β*,15*β*-dihydroxy-7,11,23-trioxolanost-8,20(22)-dien-26-oate (**17**) [28], lucidone A (**18**) [39], lucidone D (**19**) [40], lucidone E (**20**) [40], lucidone F (**21**) [40], ganoderenic acid B (**22**) [36], (3*β*,15*α*,20*E*)-3,15-dihydroxy-7,11,23-trioxolanosta-8,20(22)-dien-26-oic acid (**23**) [41], ganoderenic acid H (**24**) [42], methyl ganoderate K (**25**) [43], 7-oxo-ganoderic acid Z2 (**26**) [43], ganoderic acid *β* (**27**) [44], resinacein D (**28**) [45], (+)-(5*α*,24*E*)-3*β*,11*α*-dihydroxylanosta-8,24-dien-7-oxo-26-al (**29**) [46], 3*β*,7*β*-dihydroxy-11,15,23-trioxo-lanost-8,16-dien-26-oic acid (**30**) [47], 3*β*,7*β*-dihydroxy-11,15,23-trioxo-lanost-8,16-dien-26-oic acid methyl ester (**31**) [48], and 3*β*-hydroxy-7,11,15,23-tetraoxo-5*α*-lanosta-8,16-dien-26-oic acid (**32**) [30].

2.2. Evaluation of SH-SY5Y cells viability

Compounds **1**–**32** were evaluated for their neuroprotective effects against H_2O_2-induced damage in SH-SY5Y cells, with trolox serving as the positive control. Cell viability was assessed using the MTT method. As illustrated in Fig. 5, the cell viability of the H_2O_2-treated group (49.37%) decreased significantly compared to the control group (100%). Compounds **1**–**11**, **15**–**18**, **20**, **23**–**25**, **28**–**30**, and **32** exhibited neuroprotective activities, with cell viability ranging from 52.13% to 86.97% at a concentration of 50 μmol·L^{-1}. Notably, compounds **4**, **11**, **17**, **18**, **23**, **24**, and **32** restored cell viability to 86.97%, 83.84%, 86.69%, 83.12%, 81.35%, and 83.75%, respectively, surpassing that of trolox (75.39%). Among the tested compounds, compound **4** demonstrated the most potent neuroprotective activity, while compound **3** (59.28%) showed a weak protective effect. This suggests that the C-20/C-22 double bond in **4**, absent in **3**, is an important functional group for the neuroprotective effects of these 26-carbon lanostanoids against H_2O_2-induced SH-SY5Y cell injury. Consequently, the most potent compound, **4**, was selected for further investigation of its neuroprotective effects, including analyses of cell cycle, reactive oxygen species (ROS), and apoptosis.

2.3. Cell cycle analysis

The cell cycle plays a crucial role in regulating DNA division and replication, significantly influencing cellular activities [49]. As illustrated in Figs. 6A and 6B, the H_2O_2-induced group exhibited an increase in the G_0/G_1 phase cell population from 66.14% to 74.72%, accompanied by a decrease in the S phase population from 17.71% to 10.92%, compared to the control group. This observation indicates that H_2O_2-induced DNA damage arrested SH-SY5Y cells in the G_0/G_1 phase, impeding their progression into the S phase for DNA replication and consequently inhibiting cell proliferation. Notably, SH-SY5Y cells treated with **4** did not demonstrate G_0/G_1 phase stagnation relative to the control group, suggesting that **4** effectively protected the DNA of SH-SY5Y cells from oxidative stress-induced damage.

2.4. Effect of compound *4* on intracellular ROS level

Excessive ROS production stimulates oxidative stress, which is closely associated with the progression of numerous neurodegenerative diseases [50]. The intracellular ROS level in SH-SY5Y cells was evaluated using DCFH-DA staining. As illustrated in (see Supplementary material), treatment with 800 μmol·L^{-1} H_2O_2 significantly increased ROS production in SH-SY5Y cells compared to the control group. However, pretreatment with compound **4** at concentrations of 50, 25, and 12.5 μmol·L^{-1} significantly reduced ROS generation to 138.8%, 142.6%, and 94.0%, respectively, compared to the H_2O_2-induced group (222.8%) ($P < 0.001$). These results indicate that compound **4** effectively decreases ROS production in a dose-dependent manner, contributing to the maintenance of oxidant/antioxidant balance and protecting SH-SY5Y cells from H_2O_2-induced injury.

2.5. Hoechst 33258 staining analysis

Treatment of SH-SY5Y cells with H_2O_2 induced apoptotic cell death, as evidenced by DNA fragmentation and the presence of apoptotic bodies [51]. To elucidate the protective effect of compound **4** on H_2O_2-damaged SH-SY5Y cells, morphological apoptosis was evaluated using Hoechst 33258 staining. (see Supplementary material) demonstrated that the fragmentation of cell nuclei and cell shrinkage in the H_2O_2-induced group increased significantly compared to the control group, indicating H_2O_2-induced apoptosis. However, the fragmentation of cell nuclei in SH-SY5Y cells gradually decreased as the concentration of **4** increased, suggesting that **4** attenuated H_2O_2-induced apoptosis in a dose-dependent manner.

2.6. Effect of *4* on apoptosis rate of SH-SY5Y cells

The Annexin V-FITC/PI double staining method was employed to further evaluate the influence of **4** on H_2O_2-induced apoptosis. The effects of **4** at concentrations of 50, 25, and 12.5

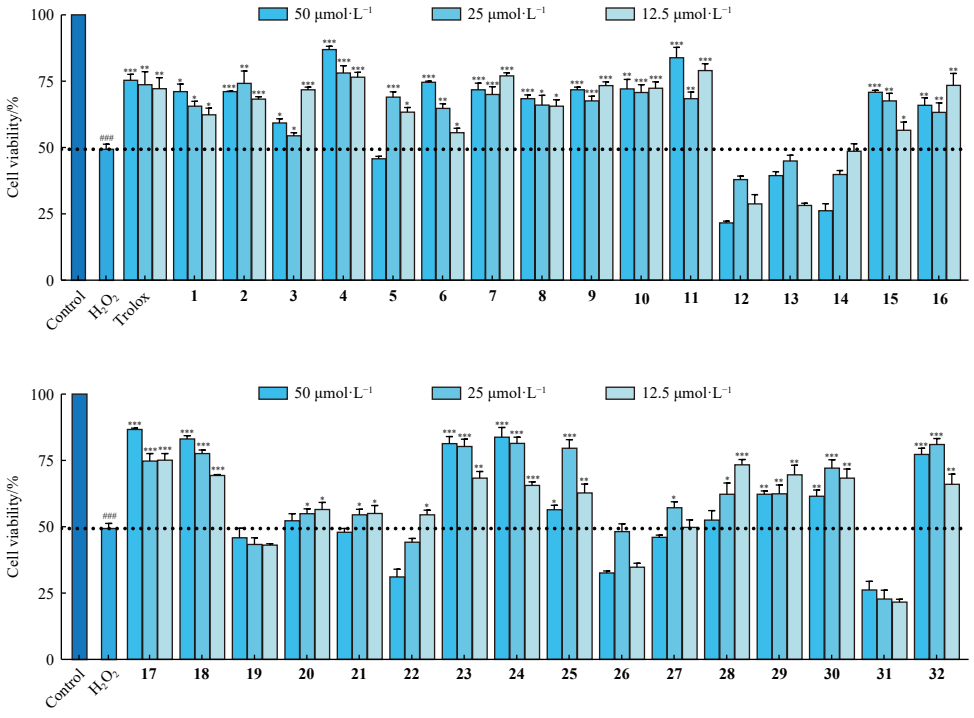

Fig. 5 The neuroprotective effects of compounds **1**–**32** against H_2O_2-induced oxidative damage in SH-SY5Y cell, as measured by MTT assay. Trolox served as a positive control. Data are presented as the mean ± SD from three independent experiments. $^{###}P < 0.001$ *vs* indicated control; $^{*}P < 0.05$, $^{**}P < 0.01$, and $^{***}P < 0.001$ *vs* the H_2O_2-induced group (800 μmol·L^{-1}).

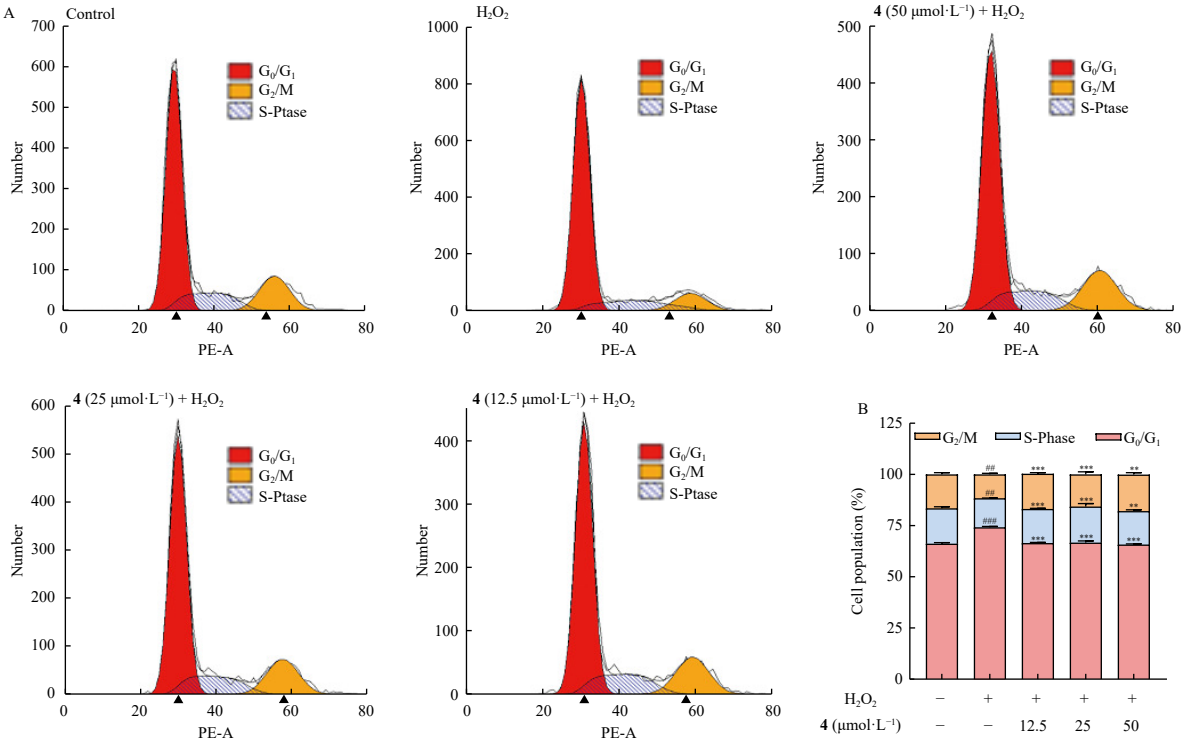

Fig. 6 Effects of compound **4** on the cell cycle of H_2O_2-treated SH-SY5Y cells. The cell cycle distribution was determined by flow cytometry (A and B). Data are presented as the mean ± SD of three independent experiments. $^{##}P < 0.01$, $^{###}P < 0.001$ *vs* indicated control; $^{**}P < 0.01$ and $^{***}P < 0.001$ *vs* the H_2O_2-induced group (800 μmol·L^{-1}).

μmol·L^{-1} on apoptosis of SH-SY5Y cells are illustrated in Figs. 7A and 7B. Compared to the control group (3.62%), the cell apoptosis rate of the H_2O_2-induced group significantly increased (21.82%), indicating that H_2O_2 induced cell apoptosis. In comparison to the H_2O_2-induced group, the apoptosis rate of SH-SY5Y cells treated with **4** decreased in a dose-dependent manner: 17.11% (12.5 μmol·L^{-1}), 10.78% (25 μmol·L^{-1}), and 8.61% (50 μmol·L^{-1}). These results suggest that **4** significantly inhibited the H_2O_2-induced apoptosis of SH-SY5Y cells, which aligns with the findings from the Hoechst 33258 staining.

2.7. Regulation of apoptosis-related proteins expression

The Bcl-2 family proteins play a crucial role in regulating cellular apoptosis, including the pro-apoptotic protein Bax and anti-apoptotic protein Bcl-2 [52]. Western blotting analyses were con-

ducted to assess the expression levels of these apoptotic proteins. As illustrated in Figs. 8A and 8B, the H_2O_2-induced group exhibited increased Bax protein expression and decreased Bcl-2 protein expression compared to the control group. Notably, SH-SY5Y cells treated with compound **4** demonstrated a significant ($P < 0.001$) decrease in Bax protein expression and a significant ($P < 0.001$) increase in Bcl-2 protein expression in a dose-dependent manner, relative to the H_2O_2-induced group. This indicates that compound **4** inhibited the cellular apoptosis process. These findings suggest that Bcl-2 family proteins are instrumental in H_2O_2-induced apoptosis, and compound **4** may protect SH-SY5Y cells against H_2O_2-induced apoptosis by modulating the protein expression levels of Bcl-2 and Bax.

2.8. PTP1B and α-glucosidase inhibitory activities evaluation

The anti-diabetic potential of the isolated compounds (**1**–**32**) was assessed through their inhibitory activities against PTP1B and α-glucosidase. Among these, compounds **26**, **12**, and **28** demonstrated inhibitory effects on PTP1B with IC_{50} values of 13.92 ± 0.54, 32.17 ± 0.87, and 56.94 ± 1.41 μmol·L^{-1}, respectively, in comparison to the positive control Na_3VO_4 (IC_{50}, 18.15 ± 0.15 μmol·L^{-1}). Notably, the PTP1B inhibitory activity of compound **26** (IC_{50}, 13.92 μmol·L^{-1}), which features a carboxyl group at C-26 instead of a methylol in **12**, was approximately twice as potent as that of **12** (IC_{50}, 32.17 μmol·L^{-1}). This observation suggests that the presence of a carboxyl group at C-26 enhances the inhibitory activity towards PTP1B.

Compound **12** demonstrated superior inhibitory activity against α-glucosidase with an IC_{50} value of 43.56 ± 1.67 μmol·L^{-1} compared to the positive control acarbose (IC_{50}, 317.2 ± 0.83 μmol·L^{-1}), while other compounds showed no activity. Among all the isolates, compound **12** is the only structure with a hydroxylated methine group at C-26, exhibiting a stronger inhibit-

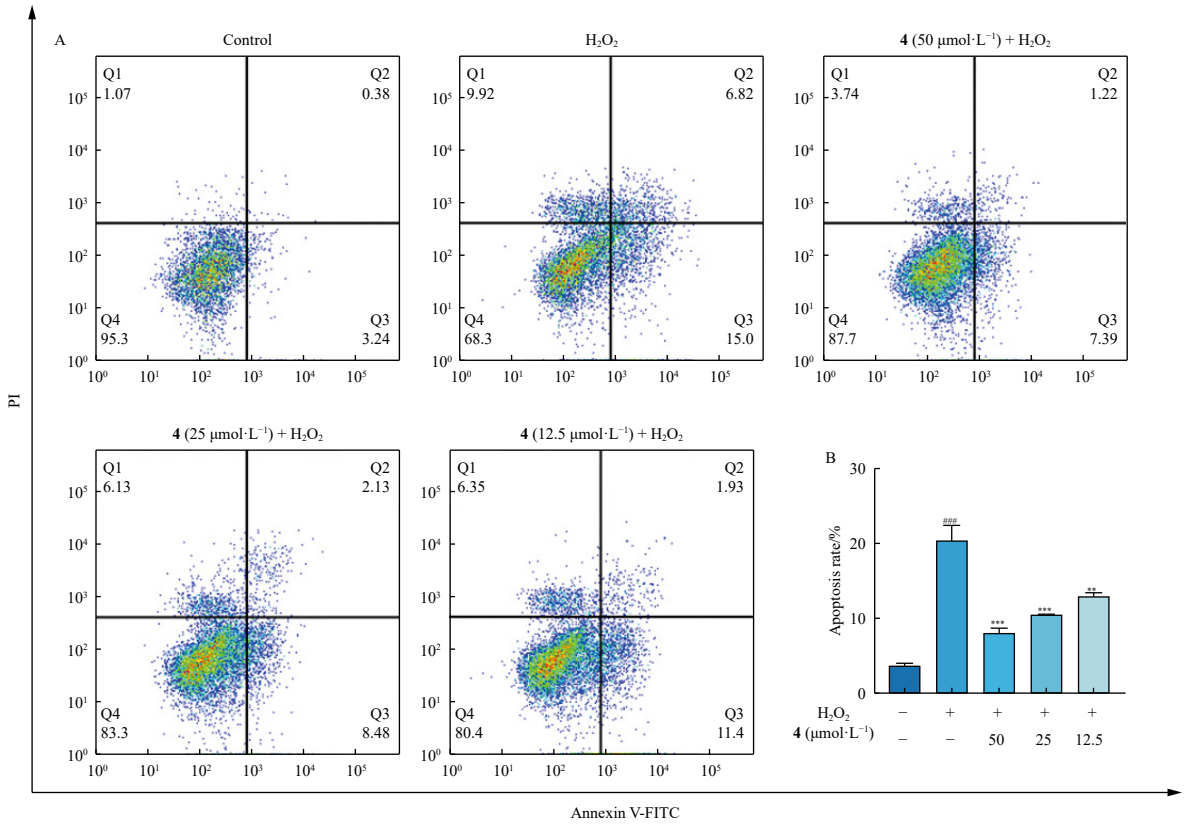

Fig. 7 The cytoprotective effect of compound **4** on H_2O_2-induced apoptosis in SH-SY5Y cells. The apoptosis rate was quantified using flow cytometry (A and B). Data are presented as mean ± SD from three independent experiments. $^{###}P < 0.001$ *vs* control; $^{**}P < 0.01$ and $^{***}P < 0.001$ *vs* the H_2O_2-treated group.

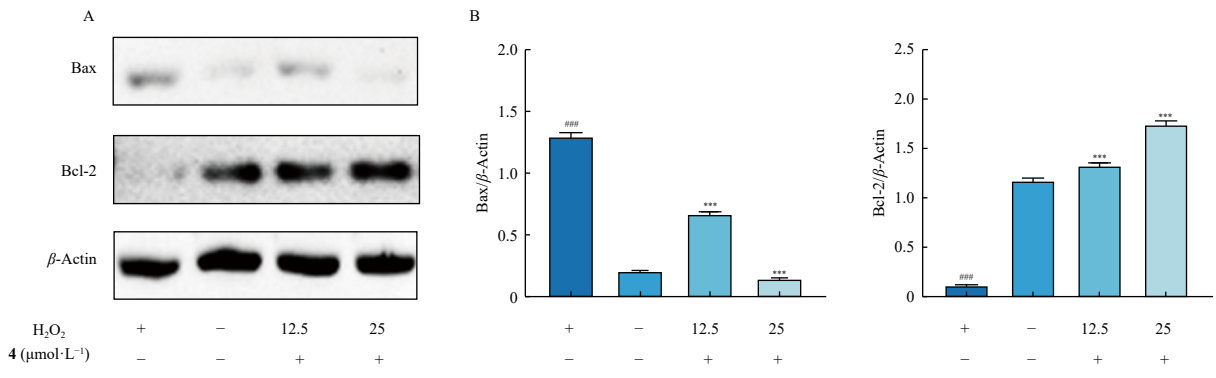

Fig. 8 Effects of **4** on apoptosis-related proteins. Immunoblot analysis of the apoptosis-related molecules in SH-SY5Y cells (A). Densitometric analysis of Bax and Bcl-2 expression levels (B). Data are presented as the mean ± SD of three independent experiments. $^{###}P < 0.001$ *vs* indicated control; $^{***}P < 0.001$ *vs* the H_2O_2-induced group.

ory effect against α-glucosidase than compound **26** (30.55% inhibition at 200 μmol·L^{-1}). This suggests that the presence of a hydroxylated methine group at C-26 may contribute to a potent α-glucosidase inhibitory activity.

2.9. Kinetic analysis and molecular docking

To further elucidate the inhibition mechanisms of the most potent compounds **26** and **12** against PTP1B and α-glucosidase, respectively, kinetic analyses and molecular docking simulations were conducted.

Kinetic analysis using the Lineweaver-Burk plot demonstrated that the lines of compounds **12** and **26** intersected on the X-axis, indicating that **12** and **26** functioned as noncompetitive inhibitors against PTP1B and α-glucosidase, respectively. Furthermore, the inhibition constants K_i for **12** and **26** were determined through secondary plots to be 39.6 and 4.4 μmol·L^{-1}, respectively.

The binding interactions of **26** with PTP1B and **12** with α-glucosidase are depicted in Supplementary materials. In the case of **26**, the hydroxyl group at C-3 established two hydrogen bonds with residues Phe280 and Gly283, while the carbonyl group at C-26 interacted with residues Arg79 and Arg199 through salt bridge formation. Additionally, **26** engaged in hydrophobic interaction with residue Phe280. For **12** , the hydroxyl groups at C-3 and C-26 formed two hydrogen bonds with residues Thr310 and Asp325. Furthermore, **12** exhibited hydrophobic interactions with residues His280, Asp307, Pro312, and Asp325.

3. Experimental

3.1. General experimental procedures

NMR spectra were recorded on a Bruker AV-500 spectrometer (Bruker, Bremen, Germany) with TMS as an internal standard. HR-ESI-MS data were obtained using a mass spectrometer API QSTAR Pulsar (Bruker, Bremen, Germany). IR spectra were acquired on a Shimadzu UV2550 spectrophotometer (Shimadzu, Kyoto, Japan), and ECD data were collected using a MOS-500 Circular Dichroism (Biologic, Seyssinet Pariset, France). Sephadex LH-20 (40–70 μm, Merck, Darmstadt, Germany), RP-C_{18} (40–70 μm, Fuji Silysia Chemical Ltd., Aichi, Japan), and Silica gel (Qingdao Haiyang Chemical Inc., Qingdao, China) were utilized for open column chromatography. Semi-preparative high-performance liquid chromatography (HPLC) was equipped with an octadecyl silane (ODS) column (YMC-pack ODS-A, 10 mm × 250 mm, 5 μm, 4 mL·min^{-1}).

3.2. Fungal material

The fruiting bodies of *Ganoderma theaecolum* were collected in July 2019 from Qiongzhong County, Hainan Province. Professor Niankai Zeng of Hainan Normal University authenticated the specimens as *Ganoderma theaecolum*. The voucher specimens (No. 2019CBLZ02) were deposited in the Institute of Tropical Biotechnology, Chinese Academy of Tropical Agricultural Sciences.

3.3. Extraction and isolation

The specifics of the extraction and isolation procedures are provided in Supplementary materials.

Ganothenoid A (**1**), yellow oil; $[\alpha]_D^{25}$ +76 (*c* 0.1, MeOH); UV (MeOH) λ_{max} (log ε): 256 (3.80) nm; ECD (MeOH) λ_{max}($\Delta\varepsilon$): 205 (–7.73), 241 (6.59), 352 (–1.02) nm; IR (KBr) ν_{max} (cm^{-1}): 3418, 2970, 1723, 1656, 1569, 1381, 1280, 1181, 1101, and 1028; ^{1}H and ^{13}C NMR data, see Tables 1 and 2; HR-ESI-MS *m/z* [M + Na]$^+$ 471.2729 (Calcd. for $C_{26}H_{40}NaO_6$ 471.2717).

Ganothenoid B (**2**), white amorphous powder; $[\alpha]_D^{25}$ +99 (*c* 0.1, MeOH); UV (MeOH) λ_{max} (log ε): 257 (3.73) nm; ECD (MeOH) λ_{max} ($\Delta\varepsilon$): 211 (–9.47), 253 (16.18), 292 (–3.28) nm; IR (KBr) ν_{max} (cm^{-1}): 3431, 2969, 1723, 1664, 1456, 1383, 1273, 1178, and 1031; ^{1}H and ^{13}C NMR data, see Tables 1 and 2; HR-ESI-MS *m/z* [M + Na]$^+$ 469.2544 (Calcd. for $C_{26}H_{38}NaO_6$ 469.2561).

Ganothenoid C (**3**), yellow oil; $[\alpha]_D^{25}$ +70 (*c* 0.1, MeOH λ_{max} (log ε): 259 (3.69) nm; ECD (MeOH) λ_{max} ($\Delta\varepsilon$): 254 (10.75), 295 (–2.12), 358 (–0.88) nm; IR (KBr) ν_{max} (cm^{-1}): 3440, 2934, 1682, 1385, 1196, and 1035; ^{1}H and ^{13}C NMR data, see Tables 1 and 2; HR-ESI-MS *m/z* [M + Na]$^+$ 467.2425 (Calcd. for $C_{26}H_{36}NaO_6$ 467.2404).

Ganothenoid D (**4**), a yellow amorphous powder, exhibited the following properties: $[\alpha]_D^{25}$ +47 (*c* 0.1, MeOH λ_{max} (log ε): 230 (3.77), 251 (3.58), 265 (3.54) nm; ECD (MeOH) λ_{max} ($\Delta\varepsilon$): 232 (–1.95), 273 (6.41), 306 (–2.53) nm; IR (KBr) ν_{max} (cm^{-1}): 3442, 2935, 1744, 1682, 1382, 1198, and 1037. The ^{1}H and ^{13}C NMR data are presented in Tables 1 and 2. HR-ESI-MS analysis revealed *m/z* [M + Na]$^+$ 465.2267 (Calcd. for $C_{26}H_{34}NaO_6$ 465.2248).

Ganothenoid E (**5**), a yellow amorphous powder, exhibited the following characteristics: $[\alpha]_D^{25}$ +10 (*c* 0.1, MeOH λ_{max} (log ε): 232 (3.64), 254 (3.50), 268 (3.50) nm; ECD (MeOH) λ_{max} ($\Delta\varepsilon$): 220 (0.46), 237 (–0.94), 232 (1.80) nm; IR (KBr) ν_{max} (cm^{-1}): 3420, 2933, 1681, 1383, 1200, 1139, and 1027; ^{1}H and ^{13}C NMR data, see Tables 1 and 2; HR-ESI-MS *m/z* [M + Na]$^+$ 467.2393 (Calcd. for $C_{26}H_{36}NaO_6$ 467.2404).

Ganothenoid F (**6**), yellow oil; $[\alpha]_D^{25}$ +24 (*c* 0.1, MeOH λ_{max} (log ε): 248 (3.66) nm; ECD (MeOH) λ_{max} ($\Delta\varepsilon$): 228 (0.68), 246 (–0.07), 274 (2.16) nm; IR (KBr) ν_{max} (cm^{-1}): 3439, 2934, 1676, 1381, 1189, 1136, and 1031; ^{1}H and ^{13}C NMR data, see Tables 1 and 2; HR-ESI-MS *m/z* [M + Na]$^+$ 551.2979 (Calcd. for $C_{31}H_{44}NaO_7$ 551.2979).

Ganothenoid G (**7**), colorless oil; $[\alpha]_D^{25}$ +47 (*c* 0.1, MeOH λ_{max} (log ε): 243 (3.64), 267 (3.50) nm; ECD (MeOH) λ_{max} ($\Delta\varepsilon$): 241 (5.45), 267 (7.81), 347 (–0.70) nm; IR (KBr) ν_{max} (cm^{-1}): 2967, 1725, 1375, 1249, 1201, 1133, and 1032; ^{1}H and ^{13}C NMR data, see Tables 1 and 2; HR-ESI-MS *m/z* [M + Na]$^+$ 591.2939 (Calcd. for $C_{33}H_{44}NaO_8$ 591.2928).

Ganothenoid H (**8**), white amorphous powder; $[\alpha]_D^{25}$ +71 (*c* 0.1, MeOH λ_{max} (log ε): 225 (3.74), 254 (3.30), 298 (3.80) nm; ECD (MeOH) λ_{max} ($\Delta\varepsilon$): 224 (4.15), 256 (2.00), 295 (8.16), 342 (–3.70) nm; IR (KBr) ν_{max} (cm^{-1}): 3452, 2932, 1679, 1381, 1260, 1198, and 1036; ^{1}H and ^{13}C NMR data, see Tables 1 and 2; HR-ESI-MS *m/z* [M + Na]$^+$ 507.3102 (Calcd. for $C_{30}H_{44}NaO_5$ 507.3081).

3.4. Biological assays

3.4.1. Cell viability assay

All compounds underwent evaluation for neuroprotective activities using the MTT method [53]. SH-SY5Y cells were obtained from the Cell Bank of Type Culture Collection of Chinese Academy of Sciences (Shanghai, China). The cells were cultivated in MEM/F12 medium supplemented with 10% FBS (*V*/*V*) and 1% (*V*/*V*) penicillin/streptomycin in a humidified incubator with 5% CO_2 at 37 °C. Cells were inoculated in 96-well plates at a density of 1 × 10^4 cells/well. The cells were treated with tested compounds **1**–**32** (12.5, 25, and 50 μmol·L^{-1}) for 12 h and then exposed to 800 μmol·L^{-1} H_2O_2 for 12 h. Subsequently, 20 μL of 5 mg·mL^{-1} MTT was added to each well and incubated for 4 h. After removing the MTT solution, the formazan crystal products in each well were dissolved in 150 μL DMSO. Absorbance was measured using a microplate reader at 490 nm. Cell viability was expressed as a percentage relative to control cells.

3.4.2. Cell cycle assay

SH-SY5Y cells were seeded in 6-well plates for 24 h, followed

by treatment with compound **4** (12.5, 25, and 50 μmol·L^{-1}) for 12 h and subsequently with H_2O_2 for an additional 12 h. The cells were then resuspended and fixed with precooled 70% ethanol for 24 h at 4 °C. Following fixation, cells were harvested by centrifugation and resuspended in 500 μL PI/RNase staining buffer. The cell suspension was incubated with 25 μL PI (propidium iodide) and 10 μL RNase (Beyotime, Shanghai, China) for 30 min at room temperature. Cell cycle analysis was performed within 1 h using flow cytometry (Accuric 6 Plus, Becton Dickinson, USA).

3.4.3. Detection of ROS level

SH-SY5Y cells were seeded into 6-well plates. The cells underwent pretreatment with **4** (12.5, 25, and 50 μmol·L^{-1}) for 12 h accompanied with H_2O_2 for 12 h, followed by concurrent exposure to H_2O_2 for an additional 12 h. Subsequently, the cells were incubated with 10 μmol·L^{-1} DCFH-DA (Beyotime, Shanghai, China) for 30 min at 37 °C in darkness. Following incubation, the cells were harvested and resuspended in 1 mL PBS. Intracellular ROS levels were quantified using flow cytometry (Accuric 6 Plus, Becton Dickinson, USA).

3.4.4. Hoechst 33258 staining

To evaluate apoptosis morphology, Hoechst 33258 staining was performed. The SH-SY5Y cells were plated in 6-well plates for 24 h, followed by treatment with **4** (12.5, 25, and 50 μmol·L^{-1}) for another 12 h and then with H_2O_2 for 12 h. The cells were washed with PBS and stained with Hoechst 33258 staining (Beyotime, Shanghai, China) working solution, then incubated at room temperature in the dark for 10 min. Subsequently, the cell morphology was observed using a fluorescence microscope (Flash4.0, Olympus, Japan).

3.4.5. Apoptosis assay by flow cytometry

Cell apoptosis was assessed using an Annexin V-FITC/PI detection kit following the manufacturer's protocol. SH-SY5Y cells in the logarithmic growth phase were seeded in 6-well plates and incubated for 24 h. Subsequently, the cells were treated **4** (12.5, 25, and 50 μmol·L^{-1}) for 12 h, followed by H_2O_2 exposure for an additional 12 h. The cells were then harvested *via* trypsinization, washed with PBS, and centrifuged at 1000 r·min^{-1} for 5 min. The resulting cell pellet was resuspended in 500 μL of Annexin V-FITC binding solution (Vazyme, Nanjing, China). Following this, 5 μL each of Annexin V-FITC and PI were added to the cell suspension, which was then incubated at room temperature in darkness for 15 min. The stained cells were subsequently analyzed using flow cytometry.

3.4.6. Western blotting

In summary, proteins from SH-SY5Y cells were extracted and lysed using a lysis buffer. Subsequently, protein concentration was determined using a BAC Protein Samples Assay Kit (Solarbio, Beijing, China). Equal quantities of protein samples were separated by denaturing sodium dodecyl sulfate-polyacrylamide gel electrophoresis (SDS-PAGE) gel and transferred to polyvinylidene fluoride (PVDF) membranes. The membranes were then incubated with antibodies at 4 °C overnight. The intensity of the resulting bands was quantified using Image J software.

3.4.7. PTP1B inhibitory assay

The PTP1B inhibition assay of all isolated compounds was conducted using *p*-PNPP (*p*-nitrophenyl phosphate) as the substrate, following previously established methods [54]. The assay was performed in a final volume of 100 μL, utilizing a reaction buffer containing 5 mmol·L^{-1} EDTA and 5 mmol·L^{-1} NaAc, with or without test compounds. Following 15 min of incubation at 37 °C, 20 μL of *p*-NPP solution was introduced into the system, followed by an additional 30 min of incubation at 37 °C. Sodium orthovanadate (Na_3VO_4) and dimethyl sulfoxide (DMSO) served as positive and negative controls, respectively. The inhibition rates (%) were calculated using the formula: $[(OD_{control} - OD_{blank}) - (OD_{compound} - OD_{blank})]/(OD_{control} - OD_{blank}) \times 100\%$.

3.4.8. α-Glucosidase inhibitory assay

The α-glucosidase inhibitory activity was conducted following previously established protocols [3]. In brief, 100 μL of 0.2 U·mL^{-1} α-glucosidase solution (dissolved in 100 mmol·L^{-1} PBS, pH 6.8) was incubated with 10 μL of samples at varying concentrations at 37 °C for 15 min. Subsequently, 40 μL of 2.5 mmol·L^{-1} *p*-NPG was added to initiate the reaction. The absorbance was measured at 405 nm using a microplate reader. Acarbose and phosphate buffer served as the positive and negative controls, respectively.

3.4.9. Inhibition kinetic analysis

The enzyme kinetic analysis was conducted following previously established procedures [3]. The inhibition kinetics of α-glucosidase and PTP1B were assessed using various substrate concentrations of substrates (*p*-NPG at 2.5, 1.25, 0.625, and 0.313 mmol·L^{-1} for α-glucosidase; *p*-NPP at 15, 10, 5, 2.5, and 1.0 mmol·L^{-1} for PTP1B), and different concentrations of test compounds **12** and **26** (120, 100, 60, and 30 μmol·L^{-1} for **12**; 120, 100, 50, and 25 μmol·L^{-1} for **26**). The inhibition types and inhibition constants (K_i) were determined using Lineweaver-Burk plots and secondary plots, respectively.

3.4.10. Molecular docking

Molecular docking simulations were conducted using Autodock software. The three-dimensional structures of compounds **12** and **26** were constructed and optimized using the MM2 forcefield in Chem3D Pro 14.0. The crystal structures of PTP1B (PDB code: 2NT7) and α-glucosidase (PDB code: 3AJ7) were obtained from the RCSB Protein Data Bank. Water molecules and original ligands were removed, and hydrogen atoms were added to the protein using Autodock tools. Default settings were employed throughout the process. The docking results were visualized and presented using Pymol (https://pymol.org).

3.4.11. Statistical analysis

All experiments were conducted in triplicate and repeated three times (n = 3), with data reported as the mean ± SD. Statistical analyses were performed using GraphPad Prism 8.0 software, employing the two-tailed Student's *t*-test.

Funding

This work was supported by the National Natural Science Foundation of China (No. 81973568), the Earmarked Fund for China Agriculture Research System (No. CARS-21), and the Special Financial Project of the Ministry of Agriculture and Rural Areas (No. NFZX2024).

Availability of supporting information

Supporting information for this study can be obtained by contacting the corresponding authors *via* E-mail.

Declaration of competing interest

These authors have no conflict of interest to declare.

References

1 Ren L, Zhang J, Zhang T. Immunomodulatory activities of polysaccharides from *Ganoderma* on immune effector cells. *Food Chem*. 2021;340(15): 127933. https://doi.org/10.1016/j.foodchem.2020.127933.
2 Liang C, Tian D, Liu Y, et al. Review of the molecular mechanisms of *Ganoderma lucidum* triterpenoids: ganoderic acids A, C2, D, F, DM, X and Y. *Eur J Med Chem*. 2019;174(15):130-141. https://doi.org/10.1016/j.ejmech.

2019.04.039.
3 Yang L, Kong D, Xiao N, et al. Antidiabetic lanostane triterpenoids from the fruiting bodies of *Ganoderma weberianum*. *Bioorg Chem*. 2022;127:106025. https://doi.org/10.1016/j.bioorg.2022.106025.
4 Luo Q, Cao W, Cheng Y. Alkaloids, sesquiterpenoids and hybrids of terpenoid with *p*-hydroxycinnamic acid from *Ganoderma sinensis* and their biological evaluation. *Phytochem*. 2022;203:113379. https://doi.org/10.1016/j.phytochem.2022.113379.
5 Liu X, Yang L, Li G, et al. A novel promising neuroprotective agent: *Ganoderma lucidum* polysaccharide. *Int J Biol Macromol*. 2023;229(28):168-180. https://doi.org/10.1016/j.ijbiomac.2022.12.276.
6 Xu J, Xiao C, Xu H, et al. Anti-inflammatory effects of *Ganoderma lucidum* sterols *via* attenuation of the p38 MAPK and NF-κB pathways in LPS-induced RAW 264.7 macrophages. *Food Chem Toxicol*. 2021;150:112073. https://doi.org/10.1016/j.fct.2021.112073.
7 Lin Z, Zhang H. Anti-tumor and immunoregulatory activities of *Ganoderma lucidum* and its possible mechanisms. *Act Pharmacol Sin*. 2004;25:1387-1395.
8 Ren F, Meng C, Chen W, *et al*. *Ganoderma amboinense* polysaccharide prevents obesity by regulating gut microbiota in high-fat-diet mice. *Food Biosci*. 2021;42:101107. https://doi.org/10.1016/j.fbio.2021.101107.
9 Zhang Y, Wang X, Yang X, et al. Ganoderic acid A to alleviate neuroinflammation of Alzheimer's disease in mice by regulating the imbalance of the Th17/Tregs axis. *J Agric Food Chem*. 2021;69(47):14204-14214. https://doi.org/10.1021/acs.jafc.1c06304.
10 Kou R, Xia B, Wang Z, et al. Triterpenoids and meroterpenoids from the edible *Ganoderma resinaceum* and their potential anti-inflammatory, antioxidant and anti-apoptosis activities. *Bioorg Chem*. 2022;121:105689. https://doi.org/10.1016/j.bioorg.2022.105689.
11 Zhao C, Fan J, Liu Y, et al. Hepatoprotective activity of *Ganoderma lucidum* triterpenoids in alcohol-induced liver injury in mice, an iTRAQ-based proteomic analysis. *Food Chem*. 2019;271(15):148-156. https://doi.org/10.1016/j.foodchem.2018.07.115.
12 Isaka M, Chinthanom P, Sappan M, et al. Antitubercular activity of mycelium-associated *Ganoderma lanostanoids*. *J Nat Prod*. 2017;80(5):1361-1369. https://doi.org/10.1021/acs.jnatprod.6b00973.
13 Guo C, Guo D, Fang L, *et al*. *Ganoderma lucidum* polysaccharide modulates gut microbiota and immune cell function to inhibit inflammation and tumorigenesis in colon. *Carbohydr Polym*. 2021;267:118231. https://doi.org/10.1016/j.carbpol.2021.118231.
14 Liu L, Chen H, Liu C, et al. Triterpenoids of *Ganoderma theaecolum* and their hepatoprotective activities. *Fitoterapia*. 2014;98:254-259. https://doi.org/10.1016/j.fitote.2014.08.004.
15 Luo Q, Yang Z, Yan Y, et al. Ganotheaecolin A, a neurotrophic conjugated ergosterol with a naphtho[1,8-*ef*]azulene scaffold from *Ganoderma theaecolum*. *Org Lett*. 2017;19:718e721. https://doi.org/10.1021/acs.orglett.7b00012.
16 Luo Q, Li M, Luo J, et al. COX-2 and JAK3 inhibitory meroterpenoids from the mushroom *Ganoderma theaecolum*. *Tetrahedron*. 2018;74(31):4259-4265. https://doi.org/10.1016/j.tet.2018.06.053.
17 Goldsmith M, Abramovitz L, Peer D. Precision nanomedicine in neurodegenerative diseases. *ACS Nano*. 2014;8(3):1958-1965. https://doi.org/10.1021/nn501292z.
18 Moreno R, Recio J, Barber S, et al. The emerging role of mixed lineage kinase 3 (MLK3) and its potential as a target for neurodegenerative diseases therapies. *Eur J Med Chem*. 2023;257:115511. https://doi.org/10.1016/j.ejmech.2023.115511.
19 Nieoullon A. Neurodegenerative diseases and neuroprotection: current views and prospects. *J Appl Biomed*. 2011;9(4):173-183. https://doi.org/10.2478/v10136-011-0013-4.
20 Hwang S, Wang Z, Lim S. Chemo-enzymatic synthesis of vinyl and L-ascorbyl phenolates and their inhibitory effects on advanced glycation end products. *Food Chem*. 2017;214:726-735. https://doi.org/10.1016/j.foodchem.2016.07.118.
21 Hakamata W, Kurihara M, Okuda H, *et al*. Design and screening strategies for α-glucosidase inhibitors based on enzymological information. *Curr Top Med Chem*. 2009;9(1):3-12. https://doi.org/10.2174/156802609787354306.
22 Zeng L, Ding H, Hua X, *et al*. Galangin inhibits α-glucosidase activity and formation of nonenzymatic glycation products. *Food Chem*. 2019;271(15):70-79. https://doi.org/10.1016/j.foodchem.2018.07.148.
23 Zhang S, Zhang Z. PTP1B as a drug target: recent developments in PTP1B inhibitor discovery. *Drug Discov Today*. 2007;12:373-381. https://doi.org/10.1016/j.drudis.2007.03.011.
24 Goldstein B, Bittner-Kowalczyk A, White M, et al. Tyrosine dephosphorylation and deactivation of insulin receptor substrate-1 by protein-tyrosine phosphatase 1B: possible facilitation by the formation of a ternary complex with the GRB2 adaptor protein. *J Biol Chem*. 2000;275:4283-4289. https://doi.org/10.1074/jbc.275.6.4283.
25 Liu G, Zhang K. Mechanisms of the anticancer action of *Ganoderma lucidum* (Leyss. ex. Fr.) Karst. : a new understanding. *J Integr Plant Biol*. 2005;47(2):129-135. https://doi.org/10.1111/j.1744-7909.2005.00037.x.
26 Zhao X, Huo X, Dong P, et al. Inhibitory effects of highly oxygenated lanostane derivatives from the fungus *Ganoderma lucidum* on P-glycoprotein and α-glucosidase. *J Nat Prod*. 2015;78(8):1868-1876. https://doi.org/10.1021/acs.jnatprod.5b00132.
27 Ye XL. *Stereochemistry*. Beijing: Beijing University Press, 1999:257-258.
28 Li X, Liu F, Su H, et al. Twelve undescribed derivatives of ganoderic acid isolated from *Ganoderma luteomarginatum* and their cytotoxicity against three human cancer cell lines. *Phytochem*. 2021;183:112617. https://doi.org/10.1016/j.phytochem.2020.112617.
29 Su H, Wang Q, Zhou L, et al. Functional triterpenoids from medicinal fungi *Ganoderma applanatum*: a continuous search for antiadipogenic agents. *Bioor Chem*. 2021;112:104977. https://doi.org/10.1016/j.bioorg.2021.104977.
30 Chen X, Lin L, Zhao J, et al. Isolation, structural elucidation, and α-glucosidase inhibitory activities of triterpenoid lactones and their relevant biogenetic constituents from *Ganoderma resinaceum*. *Molecules*. 2018;23:1391. https://doi.org/10.3390/molecules23061391.
31 Chen H, Zhang J, Ren J, et al. Triterpenes and meroterpenes with neuroprotective effects from *Ganoderma leucocontextum*. *Chem Biodivers*. 2018;15(5):e1700567. https://doi.org/10.1002/cbdv.201700567.
32 Guo J, Yang L, Ma Q, et al. Triterpenoids and meroterpenoids with α-glucosidase inhibitory activities from the fruiting bodies of *Ganoderma austral*. *Bioorg Chem*. 2021;117:1105448. https://doi.org/10.1016/j.bioorg.2021.105448.
33 Zhang S, Wang Y, Ma Q, et al. Three new lanostanoids from the mushroom *Ganoderma tropicum*. *Molecules*. 2015;20:3281-3289. https://doi.org/10.3390/molecules20023281.
34 Hu L, Ma Q, Huang S, et al. Three new lanostanoid triterpenes from the fruiting bodies of *Ganoderma tropicum*. *J Asian Nat Prod Res*. 2013;15:357-362. https://doi.org/10.1080/10286020.2013.764869.
35 Zhang S, Ma Q, Huang S, et al. Lanostanoids with acetylcholinesterase inhibitory activity from the mushroom *Haddowia longipes*. *Phytochem*. 2015;110:133-139. https://doi.org/10.1016/j.phytochem.2014.12.012.
36 Kikuchi T, Kanomi S, Kadota S, et al. Constituents of the fungus *Ganoderma lucidum* (FR.) KARST. II.: structures of ganoderic acids F, G, and H, lucidenic acids D2 and E2, and related compounds. *Chem Pharm Bull*. 1986;34(10):4018-4029. https://doi.org/10.1248/cpb.34.4018.
37 Guo P, Wang X, Cheng Y. Three new triterpenoids from *Ganoderma petchii*. *Nat Prod Res Dev*. 2016;28(1):1-4. https://doi.org/10.16333/j.1001-6880.2016.1.001.
38 Li W, Lou L, Zhu J, et al. New lanostane-type triterpenoids from the fruiting body of *Ganoderma hainanense*. *Fitoterapia*. 2016;115:24-30. https://doi.org/10.1016/j.fitote.2016.09.010.
39 Nishitoba T, Sato H, Sakamura S. New terpenoids from *Ganoderma lucidum* and their bitterness. *Agric Biol Chem*. 1985;49:1549-1985. https://doi.org/10.1080/00021369.1985.10866944.
40 Peng X, Liu J, Han Z, et al. Protective effects of triterpenoids from *Ganoderma resinaceum* on H_2O_2-induced toxicity in HepG2 cells. *Food Chem*. 2013;141:920-926. https://doi.org/10.1016/j.foodchem.2013.03.071.
41 Komoda Y, Nakamura H, Ishihara S, et al. Structures of new terpenoid constituents of *Ganoderma lucidum* (Fr.) KARST (Polyporaceae). *Chem Pharm Bull*. 2008;33(11):4829-4835. https://doi.org/10.1248/cpb.33.4829.
42 Nishitoba T, Goto S, Sato H, et al. Bitter triterpenoids from the fungus *Ganoderma applanatum*. *Phytochem*. 1989;28:193-197. https://doi.org/10.1016/0031-9422(89)85036-8.
43 Hu L, Ma Q, Huang S, *et al*. Study on the chemical constituents from *Ganoderma tropicum*. *Chin J Med Chem*. 2013;23(2):115-119. https://doi.org/10.14142/j.cnki.cn21-1313/r.2013.02.003.
44 Min B, Nakamura N, Miyashiro H, et al. Triterpenes from the spores of *Ganoderma lucidum* and their inhibitory activity against HIV-1 protease. *Chem Pharm Bull*. 1998;46(10):1607-1612. https://doi.org/10.1248/cpb.46.1607.
45 Chen X, Zhao J, Chen L, *et al*. Lanostane triterpenes from the mushroom *Ganoderma resinaceum* and their inhibitory activities against α-glucosidase. *Phytochem*. 2018;149:103-115. https://doi.org/10.1016/j.phytochem.2018.01.007.
46 Su H, Zhou Q, Guo L, et al. Lanostane triterpenoids from *Ganoderma luteomarginatum* and their cytotoxicity against four human cancer cell lines. *Phytochem*. 2018;156:89-95. https://doi.org/10.1016/j.phytochem.2018.09.003.
47 Huang Y, Li X, Peng X, et al. NMR-based structural classification, identification, and quantification of triterpenoids from edible mushroom *Ganoderma resinaceum*. *J Agric Food Chem*. 2020;68(9):2816-2825. https://doi.org/10.1021/acs.jafc.9b07791.
48 Guan S, Yang M, Wang X, et al. Structure elucidation and complete NMR spectral assignments of three new lanostanoid triterpenes with unprecedented $\Delta^{16,17}$ double bond from *Ganoderma lucidum*. *Magn Reson Chem*. 2007;45:789-791. https://doi.org/10.1002/mrc.2046.
49 Hossain S, Lash E, Veri A, et al. Functional connections between cell cycle and proteostasis in the regulation of *Candida albicans* morphogenesis. *Cell Rep*. 2021;34:108781. https://doi.org/10.1016/j.celrep.2021.108781.
50 Galasko D, Montin T. Biomarkers of oxidative damage and inflammation in Alzheimer's disease. *Biomark Med*. 2010;4:27-36. https://doi.org/10.2217/bmm.09.89.
51 Hu X, Jiao R, Li H, et al. Antiproliferative hydrogen sulfide releasing evodiamine derivatives and their apoptosis inducing properties. *Eur J Med Chem*. 2018;151:376e388. https://doi.org/10.1016/j.ejmech.2018.04.009.
52 Wang J, Pu J, Zhang Z, et al. Triterpenoids of *Ganoderma lucidum* inhibited S180 sarcoma and H22 hepatoma in mice by regulating gut microbiota. *Heliyon*. 2023;9:e16682. https://doi.org/10.1016/j.heliyon.2023.e16682.
53 Wang L, Wang Y, Gao S, et al. Phenolic amides with anti-Parkinson's disease (PD) effects from *Nicandra physaloides*. *J Funct Foods*. 2017;31:229-236. https://doi.org/10.1016/j.jff.2017.01.045.
54 Guo J, Kong F, Ma Q, et al. Meroterpenoids with protein tyrosine phosphatase 1B inhibitory activities from the fruiting bodies of *Ganoderma ahmadii*. *Front Chem*. 2020;8:279. https://doi.org/10.3389/fchem.2020.00279.